The Astrophysical Journal, 985:9 (11pp), 2025 May 20 https://doi.org/10.3847/1538-4357/adc68e

Overall Ultra-high Energy Neutrino Emission from GRBs During Jet Expansion

Qinyuan Zhang (张秦源)[1] and Zhuo Li (黎卓)[1,2]
[1] Department of Astronomy, School of Physics, Peking University, Beijing 100871, People's Republic of China; zhangqy@stu.pku.edu.cn, zhuo.li@pku.edu.cn
[2] Kavli Institute for Astronomy and Astrophysics, Peking University, Beijing 100871, People's Republic of China
Received 2024 October 17; revised 2025 February 23; accepted 2025 March 26; published 2025 May 12

Abstract

The ultrarelativistic jet released in gamma-ray bursts (GRBs) is expected to produce ultra-high-energy cosmic rays (UHECRs), prompt gamma-ray emission, and hence prompt high-energy neutrinos by photopion interactions. In this work, we calculate the time-integrated neutrino spectrum during the expansion of jets by taking into account the time evolution of cosmic-ray and secondary spectra and neutrino production. We numerically solve the continuity equations for nucleons, pions, and muons for their spectral evolution. Since pion and muon damping weakens as the jet expands, the neutrino production at large radii at high energies may dominate that around the jet energy dissipation radius. Compared with the usually adopted approaches that only consider neutrino production around the energy dissipation radius, the overall UHE neutrino fluence integrated over time can be significantly larger, and the flavor fraction of electron neutrinos as function of neutrino energy is different at UHE, due to neutrino production at radii much larger than the energy dissipation radius. The faster magnetic field decay leads to larger UHE neutrino fluence, and the UHE neutrino spectra are weakly dependent on the energy dissipation radius and the jet Lorentz factor. Observations of prompt EeV neutrinos from GRBs by the next-generation neutrino telescopes, e.g., GRAND and IceCube-Gen2, will test the hypothesis of GRBs as UHECR sources and probe the physics of GRB jets.

Unified Astronomy Thesaurus concepts: Gamma-ray bursts (629); Neutrino astronomy (1100); Cosmic rays (329); Particle astrophysics (96)

1. Introduction

Gamma-ray bursts (GRBs) are the most violent and luminous events in the Universe, releasing huge energy in seconds (for a review, see, e.g., B. Zhang 2019). It is well established that the GRB central engine generates relativistic jets that produce prompt gamma-ray emission by internal energy dissipation (B. Paczynski & G. Xu 1994; M. J. Rees & P. Meszaros 1994), and drive relativistic external shocks into a circumburst medium that produce long-lasting afterglow emission (B. Paczynski & J. E. Rhoads 1993; P. Mészáros & M. J. Rees 1997a). GRBs are one of the main candidates for ultra-high-energy cosmic-ray (UHECR; $>10^{19}$ eV) sources (see review by, e.g., K. Kotera & A. V. Olinto 2011). Their extreme physical condition, especially the large luminosity, implies that GRBs may accelerate nuclei up to $\sim 10^{20}$ eV (e.g., M. Vietri 1995; E. Waxman 1995). Thus, GRBs are also expected to be high-energy neutrino sources, given that their intense prompt gamma-ray photons can naturally serve as targets for photopion interactions (PIs; E. Waxman & J. Bahcall 1997, 2000; K. Murase & S. Nagataki 2006), which produces pions, and followed by neutrino generation from charged pion decay, $\pi^{\pm} \rightarrow \mu + \nu_{\mu}$, and hence muon decay $\mu \rightarrow e + \nu_e + \nu_{\mu}$.

Intense efforts had been carried out to search for neutrinos from GRBs (R. Abbasi et al. 2010, 2011; IceCube Collaboration et al. 2012). However, so far, no significant correlation between neutrino events and GRBs has been found by IceCube (see the latest results by M. G. Aartsen et al. 2017; R. Abbasi et al. 2022), leading to the conclusion that the prompt-phase neutrino emission from GRBs contributes $<1\%$ of the observed diffuse neutrino flux (R. Abbasi et al. 2022). The non-detection of neutrinos, compared with correct modeling of GRB neutrino production (e.g., D. Guetta et al. 2004; S. Hümmer et al. 2012; Z. Li 2012) had made stringent constraints on GRB physics, e.g., large Lorentz factor, large radius of emission region, and/or small baryonic loading factor (H.-N. He et al. 2012; S. Hümmer et al. 2012; M. G. Aartsen et al. 2017); Thus, the non-detection of PeV neutrinos from GRBs by IceCube may not conclude that GRBs are not UHECR sources since it could be that the PIs and hence neutrino production may be inefficient. Indeed, this is an advantage for GRBs to be UHECR sources since the UHECRs do not lose energy significantly in the sources.

While PeV neutrino production had been constrained by IceCube, there is no crucial observational constraint in the EeV energy scale. The next generation neutrino telescopes with a large array using radio detection techniques, such as IceCube-Gen2 (M. G. Aartsen et al. 2021) and GRAND (J. Álvarez-Muñiz et al. 2020), are being developed, which are aiming for higher sensitivities for detecting EeV neutrinos. In theory side, GRBs are expected to produce neutrino with energy $\sim$EeV by UHECRs in the reverse shock region (E. Waxman & J. Bahcall 2000; Z. G. Dai & T. Lu 2001), in long-term afterglows (e.g., Z. Li et al. 2002), or through π^0 production and decay in the prompt emission phase (Z. Li & E. Waxman 2007). The detection of EeV neutrinos from GRBs will give direct and crucial evidence of UHECR production in GRBs. On the other hand, for neutrino production at high energies, say, far beyond PeV, the parent pions and muons may suffer strong cooling before decay, namely, the damping effect in the GRB prompt emission region. The pion damping will significantly suppress the high-energy neutrino flux (E. Waxman & J. Bahcall 1998), whereas the muon damping

modifies the neutrino flavor ratio in the source (T. Kashti & E. Waxman 2005). The observation of UHE, $\sim$EeV, neutrinos is an important probe of GRB physics since the damping depends on the physical condition of the GRB emission region.

In this work, we study the prompt high-energy neutrino emission from the GRB jets, focusing on the high-energy part of the spectrum and the flavor fraction, which may suffer from a strong damping effect. Different from the usual approach that somehow considers neutrino production within a dynamical time of the expanding jet (namely, "instantaneous approximation" hereafter; see Appendix C), we consider the evolution of the particle distribution and neutrino production rate, when the jet is expanding to radii much larger than the energy dissipation radii. This is important for the production of high-energy neutrinos as the relativistic expansion of the jet may have an impact on the damping effect, e.g., if pions and muons do not cool significantly within the limited time due to the jet expansion. We set up a model to numerically calculate the time-integrated neutrino flux from expanding GRB jets, with the damping effect and neutrino production at large radii taken into account.

This paper is organized as follows: The method for calculating PIs and the time integration of neutrino production are presented in Section 2; Numerical results of the neutrino spectrum and flavor fraction are shown in Section 3; Then, a discussion and conclusions are given in Section 4.

2. Model

We build a model for PIs in GRBs and calculate the neutrino production from charged pion decay. A simplified model is adopted from S. Hümmer et al. (2010, hereafter H10) for PIs, which helps to efficiently calculate the spectrum of secondary particles, such as pions and muons, crucial for exploring the damping effect. In the model, the continuity equations for secondary pions, muons, and hence neutrinos are solved, with the processes of production, cooling, and decay taken into account.

2.1. GRB Jet and Radiation

Consider that a relativistic jet with Lorentz factor Γ is launched from the central engine of GRB. As the jet expands, the distance of the jet from the central engine increases with time as $R \simeq \Gamma ct$, where t is the time measured in the rest frame of the jet. The thickness of the jet in the source frame is roughly $\Delta \simeq cT^{\rm ob}$, where $T^{\rm ob}$ is the observed duration of the GRB.[3] When the jet expands to $R = R_0 \gg \Delta$, corresponding to a time $t_0 = R_0/\Gamma c$, energy dissipation of the jet occurs, which produces cosmic rays and prompt gamma-ray emission. Afterward, a "shell" of gamma-ray photons propagate with the jet, and the photons continuously interact with cosmic rays within a jet crossing time of $\Gamma\Delta/c$ in the rest frame of the jet, after which photons escape and go ahead of the jet. In the jet crossing time, the jet propagates to $R \simeq R_0 + \Delta R \simeq \Delta R \simeq c\Gamma(\Gamma\Delta/c) \simeq \Gamma^2 cT^{\rm ob}$, beyond which the PI and neutrino production basically end.[4]

The dissipation radius R_0 depends on theoretical models of jets. In the kinetic energy dominated jet model, it is expected that collisions between different parts of the jet due to different velocities result in internal shocks (B. Paczynski & J. E. Rhoads 1993; M. J. Rees & P. Meszaros 1994) at radius $R_0 \simeq \Gamma^2 c\delta t$, where δt is the observed variability time reflecting the variability of the central engine. Typically, $R_0 \sim 10^{14}$ cm for $\Gamma \sim 400$ and $\delta t \sim 10$ ms. On the other hand, in the magnetically dominated jet model (P. Mészáros & M. J. Rees 1997b; M. Lyutikov & R. Blandford 2003; B. Zhang & H. Yan 2011), the energy dissipation due to, e.g., magnetic reconnection, is expected to take place at a larger radius, $R_0 \gtrsim 10^{16}$ cm.

The observed spectrum of the prompt gamma-ray photons usually follows the Band function (D. Band et al. 1993), i.e., a low-energy power law $\epsilon^{-\alpha}$ transits smoothly to the other power law at high energies, $\epsilon^{-\beta}$, around the break energy ϵ_b. Here, ϵ and ϵ_b are measured in the rest frame of the jet, where the photons can be approximated to be homogeneous and isotropic. Due to the expansion of the jet, the photon density drops as $\propto R^{-2}$. In the rest frame of the jet, the number density of the prompt emission photons per unit photon energy at R can be described as

$$n_\gamma(\epsilon, R) = \begin{cases} n_0 \left(\dfrac{R}{R_0}\right)^{-2} \left(\dfrac{\epsilon}{\epsilon_b}\right)^{-\alpha} & \epsilon_{\rm min} \leqslant \epsilon \leqslant \epsilon_b \\ n_0 \left(\dfrac{R}{R_0}\right)^{-2} \left(\dfrac{\epsilon}{\epsilon_b}\right)^{-\beta} & \epsilon_b \leqslant \epsilon \leqslant \epsilon_{\rm max} \\ 0 & \text{else,} \end{cases} \quad (1)$$

where $n_0 = n_\gamma(\epsilon_b, R_0) \simeq L_\gamma/(4\pi R_0^2 c\Gamma^2 \epsilon_b^2)$, with L_γ the GRB luminosity, and $\epsilon_{\rm min}$ and $\epsilon_{\rm max}$ are the low- and high-energy cutoffs expected, e.g., due to synchrotron self-absorption and photon-photon pair production, respectively.

We will take the typical values, $\alpha = 1$, $\beta = 2$, $\epsilon_b^{\rm ob} = \Gamma\epsilon_b = 1$ MeV, $L_\gamma = 10^{52}$ erg s^{-1}, and $T^{\rm ob} = 10$ s from observations, and assume $\epsilon_{\rm min}^{\rm ob} \sim 0.1$ keV (Z. Li & E. Waxman 2008) and $\epsilon_{\rm max}^{\rm ob} \sim 10$ GeV (e.g., Z. Li & E. Waxman 2007), expected in GRB models.

Magnetic field plays an important role in the GRB energy dissipation region since the prompt emission is believed to be dominated by synchrotron radiation from accelerated electrons. The magnetic field is expected to evolve as the jet expands. We assume after R_0, the magnetic strength B in the rest frame of the jet decays with increasing R as

$$B(R) = B_0 \left(\frac{R}{R_0}\right)^{-b}. \quad (2)$$

Defining ξ_B the magnetic to gamma-ray energy ratio at R_0, B_0 can be given by $B_0 \simeq (2\xi_B L_\gamma/R_0^2\Gamma^2 c)^{1/2}$. The power-law index b describes the evolution of magnetic field strength, i.e., $b = 1$ for magnetic flux conservation, and $b = 3/2$ for magnetic energy conservation.

Cosmic rays are only produced at the energy dissipation radius R_0 by particle acceleration processes. Afterward, the cosmic rays are expected to be confined and propagate together with the jet. Assume that proton is the dominated composition of the produced cosmic rays, and as usual, assume the accelerated protons follow a flat power law with a sharp cutoff. Thus, in the rest frame of the jet, the number of accelerated protons per unit proton energy E_p at R_0 can be

[3] Hereafter, the superscript "ob" denotes the quantity measured in the observer frame.

[4] Usually, only neutrino production within a dynamical time t of the jet, i.e., around R_0 is considered. However, in this work, we consider neutrino production in a much longer time $\Gamma\Delta/c$, i.e., up to radius $\Gamma^2 cT^{\rm ob}$.

written as

$$N_p(E_p, R_0) = \begin{cases} N_0 E_p^{-2} & E_{\rm min} < E_p < E_{\rm max}, \\ 0 & \text{else.} \end{cases} \quad (3)$$

We take $E_{\rm max}^{\rm ob} = \Gamma E_{\rm max} = 10^{21}$ eV as the maximum energy, and the minimal energy should be larger than the proton rest mass, $E_{\rm min} \gtrsim 1$ GeV. Here, the normalization N_0 should satisfy $E_\gamma f_p = \Gamma \int_{E_{\rm min}}^{E_{\rm max}} E_p N_p(E_p, R_0)\, dE_p$, where $E_\gamma \simeq L_\gamma T^{\rm ob}$ is the gamma-ray energy of the GRB and f_p is the baryonic loading factor, e.g., the ratio between the energies of accelerated protons and gamma-ray emission. The spectrum of protons will evolve due to energy loss, as discussed in Section 2.2.

2.2. PIs and Nucleon Spectral Evolution

In the rest frame of the jet, the PIs between the accelerated protons and the photons of prompt emission lead to pion production and hence neutrino production from pion decay. There are several channels of pion production in PIs. One of the main channels is the Δ resonance, $p + \gamma \rightarrow \Delta^+ \rightarrow p' + \pi$, where the produced neutrinos carry an energy of $E_\nu \sim E_p/20$ each, and there is an approximate relation between the proton energy and the target photon energy, $E_p^{\rm ob} \epsilon^{\rm ob} \simeq 0.2\Gamma^2\,{\rm GeV}^2$. However, for neutrino production at high energies, the contribution from the multi-pion channel becomes more important. In order for careful calculation of high-energy neutrino production, we should consider all production channels, especially the multi-pion channel. Here, we follow a simplified model, namely, the Sim-B model from H10, for the PI calculation, containing resonant, direct, and multi-pion channels.

Once provided the proton and photon spectra, $N_p(E_p, R)$ and $n_\gamma(\epsilon, R)$, respectively, we can calculate the production rate of charged pions per unit energy interval at pion energy E_π and radius R, $Q_\pi(E_\pi, R)$ via Equation (A1) in Appendix A for $R \leqslant \Gamma^2 c T^{\rm ob}$. The calculation of the production rate of charged pions sums up all π^+'s and π^-'s because we are only concerned with the total production, including both neutrinos and anti-neutrinos. Moreover, in the PI process, protons and neutrons may be converted to each other, but we treat protons and neutrons the same in calculating the pion production.

Note, we take $Q_\pi(E_\pi, R) = 0$ for $R \gtrsim R_{\rm over} = \Gamma^2 c T^{\rm ob}$ because the number density of prompt photons in the jet drops significantly.

We should treat protons and neutrons together. The evolution of nucleon, including protons plus neutrons, spectrum, $N_p[E_p, R(t)]$, should be solved by the continuity equation for nucleons, with the initial proton spectrum given in Equation (3),

$$\frac{\partial}{\partial t} N_p + \frac{\partial}{\partial E_p}(\dot{E}_p N_p) = 0, \quad (4)$$

where $\dot{E}_p$ is the energy-loss rate of protons. We consider particle cooling due to PIs of protons and neutrons, adiabatic expansion of plasma, and synchrotron radiation; thus, $\dot{E}_p = -E_p t_{p,\rm cool}^{-1}$, with the proton cooling time (inversed) being

$$t_{p,\rm cool}^{-1}(E_p, R) = t_{p\gamma}^{-1}(E_p, R) + t_{p,\rm ad}^{-1}(E_p, R) + t_{p,\rm syn}^{-1}(E_p, R). \quad (5)$$

The first term on the right-hand side accounts for PIs. As we treat protons and neutrons the same, the PI is simplified to be a cooling process. The cooling rate $t_{p\gamma}^{-1}(E_p, R)$ is given in Appendix A.

Next, consider adiabatic cooling. For charged particles confined in the expanding plasma, the adiabatic cooling timescale should be about the dynamical timescale, $t_{\rm ad} \simeq t_{\rm dyn} = R/\Gamma c$. However, neutrons are produced in the PIs, and without being charged, are not confined in the plasma. In the case of efficient PIs with $t_0 \gg t_{p\gamma}(R_0)$, there will be about half of secondary nucleons that are neutrons; on the contrary, when $t_0 \ll t_{p\gamma}(R_0)$, nearly all the nucleons are protons. Therefore, we modify the adiabatic cooling rate by a factor of $1 - f_\pi(E_p)/2$, where $f_\pi(E_p) = \min\{t_0/t_{p\gamma}(E_p, R_0), 1\}$, i.e.,

$$t_{p,\rm ad}^{-1}(E_p, R) = \left[1 - \frac{f_\pi(E_p)}{2}\right] t_{\rm dyn}^{-1}(R). \quad (6)$$

Finally, the last term is for synchrotron cooling of protons and neutrinos, which indeed has a negligible effect under the physical conditions concerned (see Section 3).

2.3. Time-evolving Pion and Muon Spectra and Neutrino Production

The charged pions, $\pi^\pm$'s, produce muons and electron neutrinos in their chain decays: $\pi \rightarrow \mu + \nu_\mu$; and $\mu \rightarrow e + \nu_\mu + \nu_e$. Consider the production, decay, and cooling processes of pions and muons in the rest frame of the GRB jet. The evolution of the pion and muon spectra, $N_\pi(E_\pi, R)$ and $N_\mu(E_\mu, R)$, respectively, should be solved out by their continuity equations,

$$\frac{\partial}{\partial t} N_x + \frac{\partial}{\partial E_x}(\dot{E}_x N_x) = Q_x - \frac{N_x}{\tau_x}, \quad (7)$$

where $x = \pi$ or μ, Q_x is the production rate of pions or muons, τ_x is the decay timescale of pions or muons, and $\dot{E}_x$ is the energy-loss rate. Synchrotron and adiabatic cooling is the dominant processes for the energy loss of pions and muons; thus, we have $\dot{E}_x = -E_x/t_{x,\rm cool}$, where the cooling time is given by

$$t_{x,\rm cool}^{-1}(E_x, R) = t_{x,\rm syn}^{-1}(E_x, R) + t_{\rm dyn}^{-1}(R), \quad (8)$$

with the synchrotron cooling time being $t_{x,\rm syn}^{-1} = c\sigma_{{\rm T},x} E_x B^2/6\pi m_x^2 c^4$, where the Thomson cross section for pions or muons is $\sigma_{{\rm T},x} = (8/3)\pi(e^2/m_x c^2)^2$, with m_x the rest mass. We should ignore inverse Compton (IC) scatterings for energy loss of particles here, because for muons and pions with energy $E_x^{\rm ob} = \Gamma E_x \gtrsim 100$ PeV, the factor $E_x \epsilon_b/(m_x c^2)^2 \gtrsim 10$, indicating strong Klein–Nishina suppression so that IC cooling is much weaker than synchrotron cooling. As for the decay of pions and muons, the decay times in the rest frame of the jet are $\tau_\pi = E_\pi \tau_{\pi,0}/m_\pi c^2$ and $\tau_\mu = E_\mu \tau_{\mu,0}/m_\mu c^2$, where $\tau_{\pi,0} = 2.6 \times 10^{-8}$ s and $\tau_{\mu,0} = 2.2 \times 10^{-6}$ s are the lifetimes of corresponding particles in their rest frame.

With the evolution of pion production rate Q_π (given in Section 2.2 and Appendix A), one can derive pion spectrum N_π from Equation (7) (with $x = \pi$).

Next, consider muon production rate Q_μ, as well as the production rates of neutrinos Q_{ν_μ} and Q_{ν_e}. They are all secondaries from the decay of some parent particles. In a decay chain, $a \rightarrow b$, where the secondary particle b is generated by the decay of ultrarelativistic parent particle a, the production

rate of b, $Q_b = Q_{a\to b}$, can be calculated as

$$Q_{a\to b}(E_b, R) = \int dE_a \frac{N_a(E_a, R)}{\tau_a(E_a)} p_{a\to b}(E_b; E_a), \quad (9)$$

where τ_a is the decay time of parent particles (in the rest frame of the jet), and $p_{a\to b}(E_b; E_a)$ is the probability distribution function of secondary particle b. The forms of $p_{\pi\to\mu}$, $p_{\pi\to\nu_\mu}$, $p_{\mu\to\nu_\mu}$, and $p_{\mu\to\nu_e}$ are shown in Appendix B. Note, here we only consider the total flux of neutrinos and anti-neutrinos and will not treat them separately. With the derived pion spectrum, Q_μ can be obtained (Equation (9)), and inserted into Equation (7) ($x = \mu$) to derive the evolving muon spectrum. Hence, the production rates of electron and muon neutrinos, $Q_{\nu_e}(E_\nu, R) = Q_{\mu\to\nu_e}(E_\nu, R)$ and $Q_{\nu_\mu}(E_\nu, R) = Q_{\pi\to\nu_\mu}(E_\nu, R) + Q_{\mu\to\nu_\mu}(E_\nu, R)$, respectively, can be calculated by Equation (9) using already derived pion and muon spectra.

The neutrino spectra at radius R should be integration from initial time t_0 up to time $t(R) = R/\Gamma c$. The muon and electron neutrino spectra (neutrino number per unit neutrino energy in the rest frame of the jet) at R are, respectively,

$$N_{\nu_\mu}(E_\nu, R) = \int_{t_0}^{t(R)} dt_i Q_{\nu_\mu}(E_\nu, R_i), \quad (10)$$

and

$$N_{\nu_e}(E_\nu, R) = \int_{t_0}^{t(R)} dt_i\, Q_{\nu_e}(E_\nu, R_i), \quad (11)$$

with $R_i = \Gamma c t_i$. To calculate the total neutrino number spectrum, $N_\nu(E_\nu)$, the upper bound of the integrals in the above two equations should be the time (or radius) where all the produced muons decay. The observed time-integrated neutrino flux as a function of neutrino energy, i.e., fluence spectrum, can be obtained as

$$\Phi_\nu(E_\nu^{\rm ob}) = \frac{N_\nu(E_\nu)}{\Gamma 4\pi d_L^2}, \quad (12)$$

where $E_\nu = E_\nu^{\rm ob}/\Gamma$, and d_L is the luminosity distance of the GRB.

In Equation (7), both radiative cooling and decay have been taken into account in the evolution of pion and muon distributions, so the damping effects have been considered for neutrino production. However, different from the approach of instantaneous approximation (see Appendix C for details) for pion and muon distributions, we consider their time-evolution during the jet expansion, and obtain the final neutrino spectrum and flavor fraction by summing up contributions of all times and radii.

3. Results

To solve the continuity equations, Equations (4) and (7), for the time-dependent spectra of muons and pions, we use the fully implicit difference scheme (M. Chiaberge & G. Ghisellini 1999), which can find stable and accurate solutions with fewer mesh points. Hereafter, we will take the following parameter values as fiducial ones, unless stated otherwise: $\Gamma = 400$, $R_0 = 10^{14}$ cm, $b = 1$, $\xi_B = 1$, and $f_p = 10$.

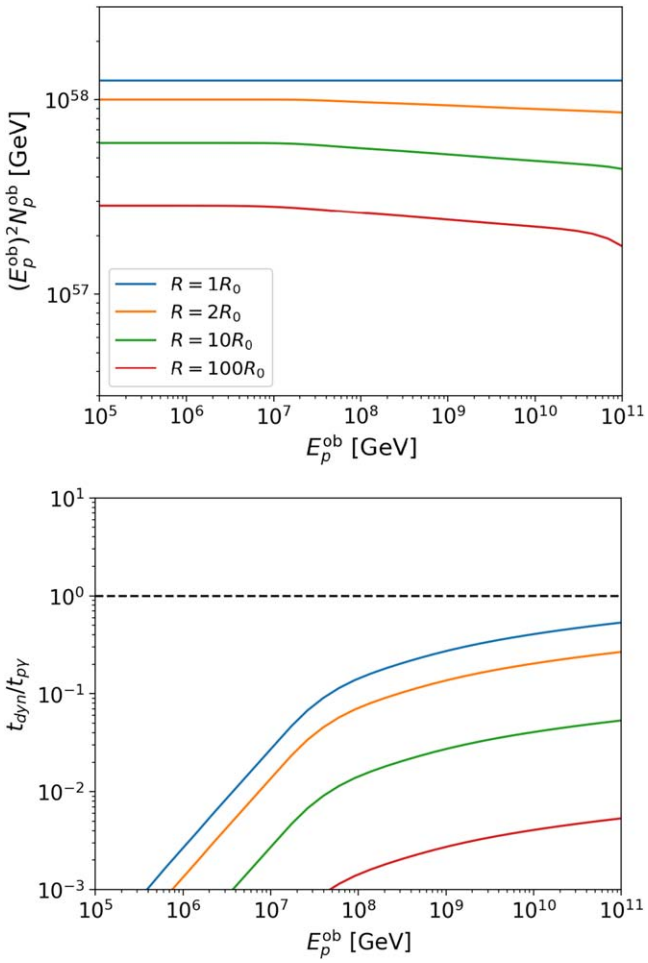

Figure 1. The nucleon spectrum (upper panel) and the ratio $t_{\rm dyn}/t_{p\gamma}$ as a function of nucleon energy (lower panel), evolving with jet radius R. Fiducial parameter values are used (see the text).

3.1. Time-dependent Spectra of Parent and Secondary Particles

We first show the results about how the spectra of parent particles and secondary products evolve with time, or radius, as the jet is expanding. Figure 1 presents the evolution of the spectrum of nucleons, i.e., protons plus neutrons, during the expansion of the jet in the case of fiducial parameter values. The upper panel shows the spectra of nucleons in the observer frame, $(E_p^{\rm ob})^2 N_p^{\rm ob}(E_p^{\rm ob}, R) = \Gamma E_p^2 N_p(E_p, R)$, at different radii. As the spectrum of nucleons is determined by the cooling process of nucleons, which is in turn determined by the PI and adiabatic cooling (Equation (5)), we present in the lower panel of Figure 1 the ratio $t_{\rm dyn}(R)/t_{p\gamma}(E_p, R)$ at different radii. This ratio defines an "optical depth of protons" due to PIs.

With fiducial parameter values, the optical depth is initially smaller than unity across the energy range concerned, i.e., the "optically thin" case. As the photon number density decreases as $n_\gamma \propto R^{-2}$, $t_{p\gamma}^{-1} \propto R^{-2}$, the ratio $t_{\rm dyn}/t_{p\gamma} \propto R^{-1}$ decreases. So this case is always with $t_{\rm dyn}/t_{p\gamma} < 1$ (lower panel of Figure 1), implying that the cooling by PIs does not affect the nucleon spectrum significantly. Thus, the adiabatic cooling should dominate the nucleon spectral evolution, leading to an energy-independent decrease in nucleon flux. As seen in Figure 1, at $R \lesssim 2R_0$ the spectrum does not change significantly, and only at

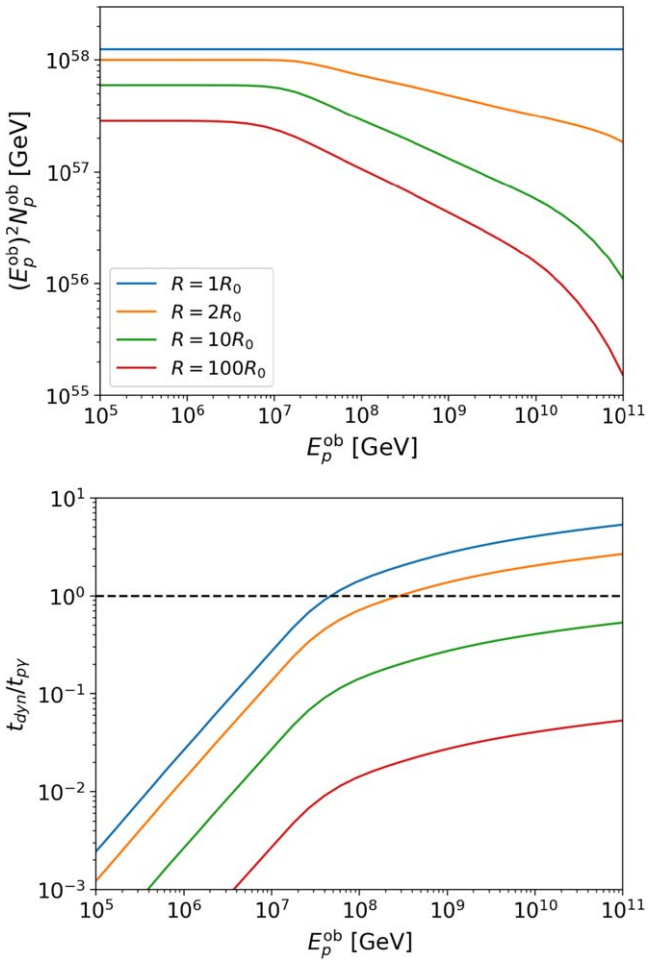

Figure 2. Same as Figure 1, but with $R_0 = 10^{13}$ cm.

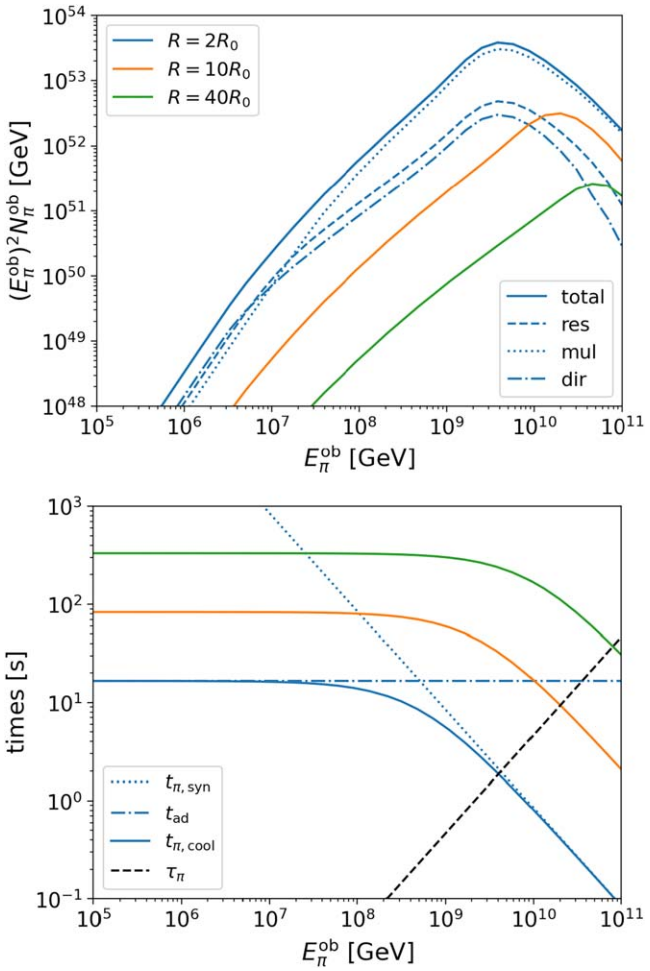

Figure 3. The charged pion spectrum (upper panel) and the cooling and decay time of charged pions as functions of pion energy (lower panel) evolving with jet radius R. For $R = 2R_0$ the contributions of pion production by resonant, direct, and multi-pion channels and the synchrotron and adiabatic cooling times of charged pions are shown for examples.

$R \gtrsim 10R_0$ the spectrum moves significantly below, but with the spectral shape largely unchanged.

For comparison, we show in Figure 2 the spectra of nucleons in an "optically thick" case with much smaller initial radius, $R_0 = 10^{13}$ cm. We can see in the lower panel of Figure 2 that the timescale ratio is initially larger than unity for nucleons with energy $E_p^{ob} \gtrsim 10^7$ GeV, i.e., the cooling through PIs is significant for the highest-energy nucleons at the beginning. At $R = 2R_0$, the strong cooling results in significant spectral steepening at high energies since the cooling rate $t_{p\gamma}^{-1}$ increases with E_p. High-energy nucleons continue cooling fast by PIs until the ratio decreases to $t_{dyn}/t_{p\gamma} < 1$ across all nucleon energies at $R \gtrsim 10R_0$. After that, the nucleon number decreases with the spectral profile remaining unchanged (upper panel of Figure 2). The much steeper nucleon spectrum at large radii compared to the optically thin case will result in suppression of neutrino production (discussed in Section 3.2).

Next, we present in Figures 3 and 4 the evolution of the spectra of the produced pions and muons. For the pion spectrum in Figure 3, the contribution from different types of channels for pion production is shown. In the upper panel of Figure 3, a break around $E_{\pi,b}^{ob} \sim 10^7$ GeV can be found in the pion spectrum from the resonant channel at $R = 2R_0$. This break is caused by a corresponding spectral break ϵ_b in the photon spectrum (Equation (1)), leading to that the pion production rate from the resonant channel follows $E_\pi^2(Q_\pi)_{res} \propto E_\pi^{\beta-1} \propto E_\pi$ for pions below the break energy and $E_\pi^2(Q_\pi)_{res} \propto E_\pi^{\alpha-1} \propto E_\pi^0$ for the above. The spectrum of produced pions is then $E_\pi^2(N_\pi)_{res} \sim E_\pi^2(Q_\pi)_{res}\tau_\pi \propto E_\pi^2$ and $\propto E_\pi$, below and above the break energy, respectively. Above $E_{\pi,b}^{ob}$, the pion contribution from the multi-pion channel, as can be seen, increases faster than that from the resonant and direct channels and becomes dominant at high energies. As a result, the total pion spectrum becomes smoother around the spectral break at $E_{\pi,b}^{ob}$.

As $t_{dyn}/t_{p\gamma} \propto R^{-1}$, pion production is dominated by PIs around R_0 in either the optically thin or optically thick cases. Afterward, the pion number decreases. In the upper panel of Figure 3, one sees that as the bulk pion number is decreasing with time/radius, there is a spectral peak in the pion spectrum evolving from $10^{9.5}$ GeV to higher energies. These breaks are caused by pion damping, i.e., when the pion cooling timescale, $t_{\pi,cool} = (t_{\pi,syn}^{-1} + t_{dyn}^{-1})^{-1}$, is smaller than the decay time of pions, τ_π, pions significantly lose energy before decay. Denote $E_{\pi,damp}^{ob}(R)$ as the pion damping energy, where the cooling and decay times are equal, $t_{\pi,cool} = \tau_\pi$. As shown in the lower panel of Figure 3, due to the short decay time of pions, the damping energy is determined by comparing the synchrotron cooling time with the decay time. For the case of fiducial parameter

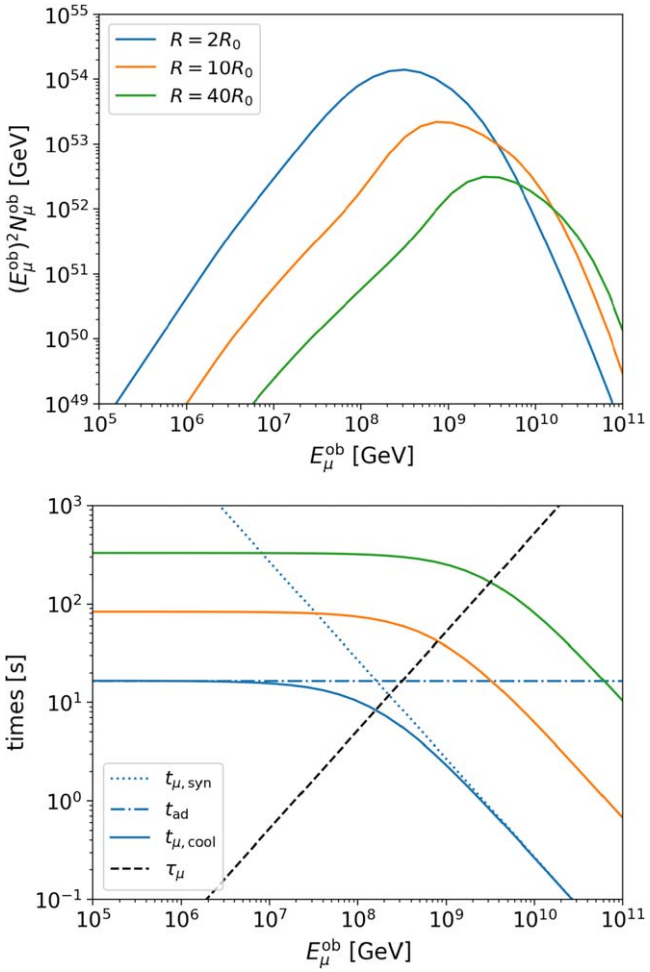

Figure 4. Same as Figure 3, but for muons.

values, the magnetic field decays as $B \propto R^{-1}$; thus, as shown in the lower panel, the pion damping energy at R_0 is $E^{\rm ob}_{\pi,\rm damp}(R_0) \sim 10^{9.5}$ GeV (which is consistent with other analytical estimates, e.g., K. Murase et al. 2012), and evolves as $E^{\rm ob}_{\pi,\rm damp} \propto R$. So the spectral break appears at higher energy for larger radius, and hence PIs at larger radii may significantly contribute to production of high-energy neutrinos, see below.

Pion decay produces muons, whose spectral evolution is shown in Figure 4. Two spectral breaks show up in the muon spectrum. The relatively low-energy one, which is also the spectral peak, is due to muon damping, corresponding to the muon damping energy $E_{\mu,\rm damp}$, where the muon cooling time is equal to the muon decay time, $t_{\mu,\rm cool} = \tau_\mu$. As the muon decay time is much larger than that of pions, the muon damping energy is much lower than that of pions, $E^{\rm ob}_{\mu,\rm damp}(R_0) \sim 10^8$ GeV (see the lower panel of Figure 4). One sees that at $E_{\mu,\rm damp}$, the muon synchrotron cooling time is comparable to the adiabatic cooling time, and hence, adiabatic cooling cannot be ignored. However, for muons with larger energies, synchrotron cooling becomes dominant.

The other spectral break appears at relatively high energy in the muon spectrum, beyond which the muon spectrum steepens sharply (upper panel of Figure 4). This break results from the pion damping effect, $E_{\mu,c} \sim (3/4)E_{\pi,\rm damp}$, above which muon production is suppressed significantly, and the flux sharply declines with muon energy due to pion and muon damping together. Note, in the upper panel of Figure 4, the muon flux at

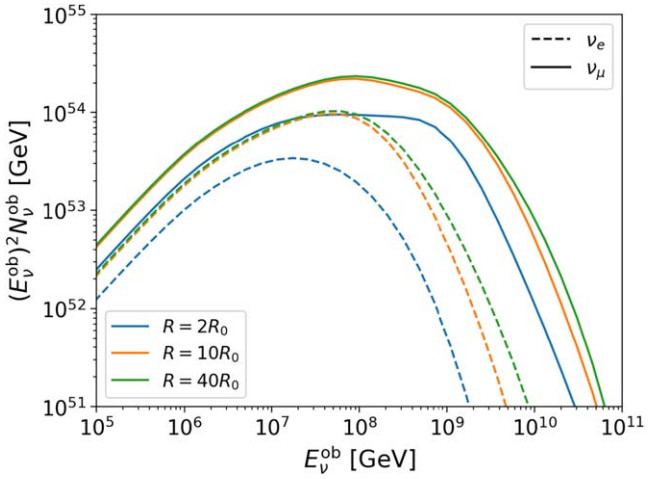

Figure 5. The neutrino spectrum evolving with jet radius R. The dashed and solid lines represent electron and muon neutrinos, respectively.

the highest energies is larger at larger radius. This is because of the fast increase in pion damping energy $E_{\pi,\rm damp} \propto R$, and hence, the break energy $E_{\mu,c} \propto R$, leading to more muon production at large radii.

Finally, Figure 5 shows the evolution of the neutrino spectrum during the expansion of the jet. We calculate the cumulative neutrino spectrum up to R, $N_\nu^{\rm ob}(E_\nu^{\rm ob}, R)$, with the method described in Section 2.3. Since the interaction rate decreases rapidly with radius, $t_{p\gamma}^{-1} \propto R^{-2}$, the integration for neutrino number roughly gives $N_\nu \propto (1 - R_0/R)$, neglecting the damping effect. So the neutrino production is almost completed at $R \sim 10R_0$ for neutrinos with energy lower than the corresponding damping energies, which is the muon damping energy $E^{\rm ob}_{\mu,\rm damp}(R_0)/3 \sim 10^{7.5}$ GeV for electron neutrinos and pion damping energy $E^{\rm ob}_{\pi,\rm damp}(R_0)/4 \sim 10^9$ GeV for muon neutrinos. However, production at larger radii is still non-negligible for neutrinos with energy larger than the corresponding damping energy (see Figure 5).

3.2. Neutrino Fluence Spectrum

By integration up to a large radius, say, $R = 10^4 R_0$, we obtain the total neutrino fluence, assuming $d_L = 100$ Mpc, hereafter. Figure 6 shows the total fluence spectrum $(E_\nu^{\rm ob})^2\Phi_\nu$ of all-flavor neutrinos, as well as the contribution from different pion production channels. As is well known, in the resonant channel, a spectral break corresponding to the gamma-ray spectral break, $\epsilon_b^{\rm ob} = 1\epsilon^{\rm ob}_{b,\rm MeV}$ MeV, should show up at neutrino energy $E_\nu^{\rm ob} \sim (1/20)\Gamma m_p c^2 \epsilon_\Delta/2\epsilon_b \sim 10^6 \Gamma^2_{400}(\epsilon^{\rm ob}_{b,\rm MeV})^{-1}$ GeV ($\epsilon_\Delta \sim 0.3$ GeV for resonance), which can be seen in Figure 6. Below this break, the resonant and direct channels contribute most neutrinos, and the fluence increases as $(E_\nu^{\rm ob})^2\Phi_\nu \propto E_\nu^{\rm ob}$, corresponding to the photon spectral slope of $n_\gamma \propto \epsilon^{-2}$ for $\epsilon > \epsilon_b$. From Figure 6, one can find that the neutrinos with $E_\nu^{\rm ob} \gtrsim 10^{6.5}$ GeV mainly result from the multi-pion channel. There are two more spectral breaks that appear in this energy range: one is $E_\nu^{\rm ob} \sim E^{\rm ob}_{\mu,\rm damp}(R_0)/3 \sim 10^{7.5}$ GeV (lower panel in Figure 4), corresponding to muon damping; the other is $E_\nu^{\rm ob} \sim E^{\rm ob}_{\pi,\rm damp}(R_0)/4 \sim 10^9$ GeV (lower panel in Figure 3), caused by pion damping. These features in the spectrum result from synchrotron cooling of charged particles, and the measurement of them could be important probes of the jet physics, e.g., the magnetic field.

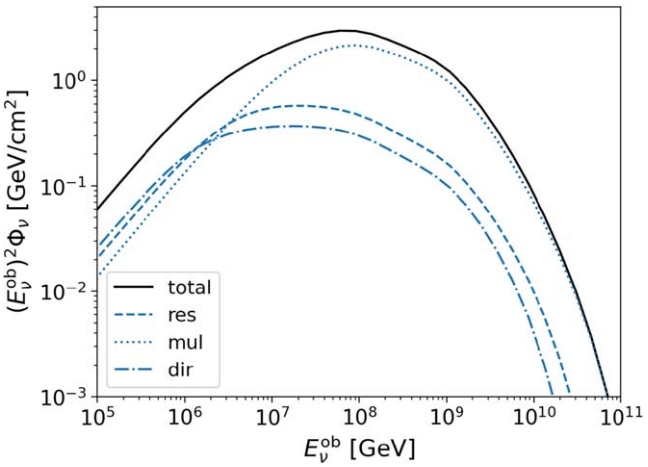

Figure 6. All-flavor neutrino fluence spectra: the total fluence (solid line) and the contributions from resonant (dashed line), multi-pion (dotted line), and direct (dashed–dotted line) channels.

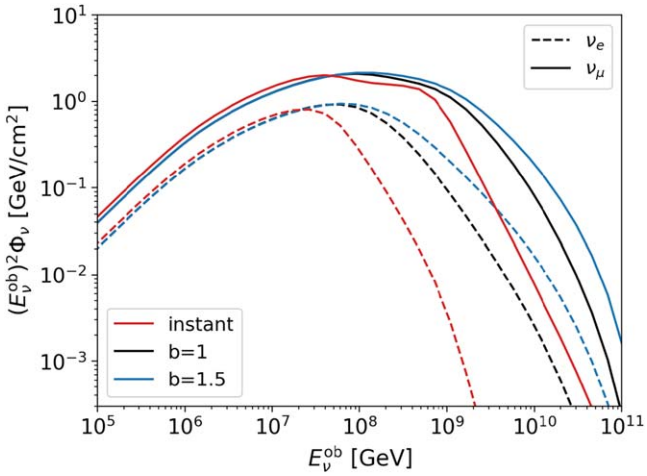

Figure 7. Neutrino fluence spectra with different magnetic field decay indices, $b = 1$ (black line) and 1.5 (blue line), in comparison with that of the instantaneous approximation (red line).

In Figure 7, we present the impact of the magnetic field decay on neutrino spectra (before neutrino oscillation). We consider different decay index b (Equation (2)), and calculate the neutrino spectrum under instantaneous approximation for comparison. We have described in detail how the calculation is done in this approximation in Appendix C. The approximation works well below $E_\nu^{ob} \sim E_{\mu,\rm damp}^{ob}(R_0)/3$, corresponding to muon damping, only with a small difference due to the adiabatic cooling considered or not. The difference becomes significantly larger at higher energies. For electron neutrinos, the spectrum in instantaneous approximation decreases steeply, roughly as $(E_\nu^{ob})^2\Phi_\nu \propto t_{\mu,\rm cool}/\tau_\mu \propto E_\nu^{-2}$, in the energy range suffering muon damping, whereas the time-integrated spectra in this work are much shallower in the same energy range. For muon neutrinos, muon damping does not affect the spectrum significantly, but pion damping does significantly suppress the muon neutrino production. And the shape of muon neutrino spectra in the energy range suffering pion damping is similar to that of electron neutrinos suffering muon damping.

This is the impact of the neutrino contribution at large radii. As shown in Figure 5, the neutrino contribution at $R > 10R_0$ becomes more important at higher energies. This is because the damping energy increases as $\propto R^b$, then muons and pions produced at large enough radii are free from the damping effect, while they suffer a strong damping effect around R_0. For larger b, the contribution at large radii is larger, leading to a shallower neutrino spectrum.

We further examine the effects of parameters R_0 and Γ on the neutrino spectrum in Figures 8 and 9. One can see in Figure 8 that as R_0 increases, the neutrino fluence decreases and the spectrum extends to higher energies. Consider the cause below. As the photon number density decreases with R_0, $t_{p\gamma}^{-1} \propto R_0^{-2}$, and the low-energy neutrinos are mainly produced around R_0, with dynamical time $t_{\rm dyn} \propto R_0$, the fluence is then $\propto t_{p\gamma}^{-1} t_{\rm dyn} \propto R_0^{-1}$. On the other hand, since $B_0 \propto R_0^{-1}$, $E_{\pi,\rm damp}^{ob} \propto R_0$, leading to a spectral turnover at higher energy for larger R_0, i.e., the neutrino spectrum extends to higher energy.

The decrease in spectral peak is somewhat compensated with the increase in the peak energy (corresponding the muon or pion damping energy for ν_e or ν_μ, respectively), leading to comparable fluences at high energies for different R_0, except

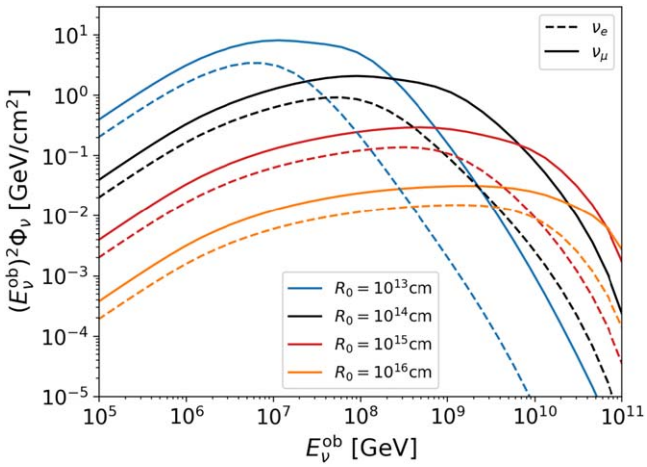

Figure 8. Neutrino fluence spectra with different initial radius R_0.

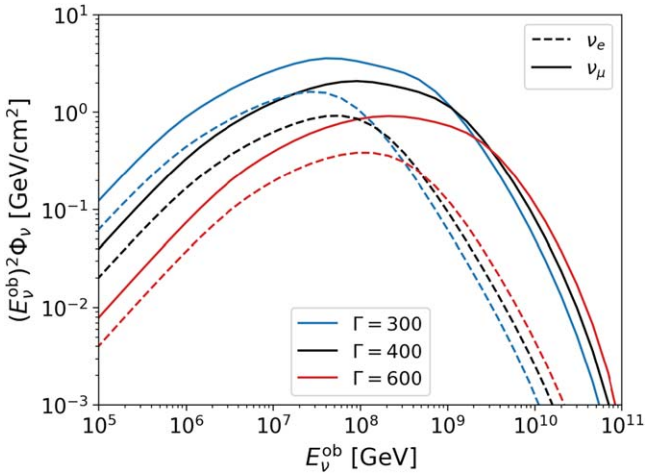

Figure 9. Neutrino fluence spectra with different jet Lorentz factor Γ.

for the case of $R_0 = 10^{13}$ cm, which is an optically thick case (Section 3.1).

In the optically thick case, the strong cooling of high-energy nucleons by PIs at small radii suppresses pion production at

large radii, where muon and pion damping is weak. Thus, for electron neutrinos and muon neutrinos above their damping energy ($E_\nu^{\rm ob} \sim 10^7$ GeV for muon damping and $E_\nu^{\rm ob} \sim 10^8$ GeV for pion damping, see Figure 8), the production is strongly suppressed. In this case, the neutrino fluence is much smaller than that with large R_0, showing a power law $\Phi_\nu \propto E_\nu^{-4}$, similar to the instantaneous approximation.

The impact of Γ on the neutrino spectrum is shown in Figure 9. It can be seen that the fluence spectrum is sensitive to Γ at low energies but not at high energies. By Figure 9, one can find that the fluence and the Lorentz factor follow a relation, $(E_\nu^{\rm ob})^2\Phi_\nu^{\rm ob} \propto \Gamma^{-4}$, in the low-energy range where the contribution of neutrinos by the resonant channel dominates. As $B_0 \propto \Gamma^{-1}$, the pion damping energy should be $E_{\pi,\rm damp} \propto \Gamma$ if synchrotron cooling dominates adiabatic cooling. The fact that the fluence decreases but the pion damping energy increases with Γ results in the neutrino fluence at high energies being very insensitive to Γ.

3.3. Neutrino Flavor Fraction

As is known, for neutrinos from the chain decay of charged pions, the neutrino flavor fractions are $(f_{e,S}:f_{\mu,S}:f_{\tau,S}) = (1/3:2/3:0)$ (Here $f_\alpha \equiv \Phi_{\nu_\alpha}/\Phi_{\nu_{\rm all}}$, $\alpha = e, \mu, \tau$; the subscript "S" denotes the flavor fraction in sources). However, if suffering strong muon damping, they become (0:1:0). In the instantaneous approximation, the flavor ratio transition happens sharply at the energy corresponding to muon damping, but in our careful consideration of the time-evolving spectrum, the case is different.

As shown in Figure 10, the transition of neutrino flavor fractions caused by muon damping occurs roughly at $E_\nu^{\rm ob} \sim 10^8$ GeV, somewhat larger than in the instantaneous approximation, $E_\nu^{\rm ob} \sim E_{\mu,\rm damp}^{\rm ob}(R_0)/3 \sim 10^{7.5}$ GeV. This is because in the time-integrated model, the production of electron neutrinos at large radii, where muon damping is not severe, is still significant, as Figure 7 shows. Then, the change of flavor fractions for the time-integrated model is slower than that of the instantaneous approximation.

There should be another critical neutrino energy that is related to pion damping. Because pion damping suppresses the muon neutrino fluence, there is a break at $E_\nu^{\rm ob} \sim E_{\pi,\rm damp}^{\rm ob}(R_0)/4 \sim 10^9$ GeV. The decrease of the electron neutrino fraction becomes slower for larger energies. In Figure 10, this break is significant in our time-integrated models due to the non-negligible electron neutrino fraction. However, in the instantaneous approximation, the electron neutrino fraction is almost zero at the pion damping energy; thus, the second critical point does not appear.

Neutrinos undergo oscillation during propagation. We show the flavor fraction when neutrinos arrive at Earth in the lower panel of Figure 10. At arrival, the flavor fraction in sources is transformed into $f_{\alpha,\oplus} = \Sigma_\beta P_{\beta\alpha} f_{\beta,S}$, where $P_{\beta\alpha} = \Sigma_i |U_{\beta i}||U_{\alpha i}|$ is the average flavor transition probability, and U is the lepton mixing matrix. We adopt the best-fit values of the neutrino mixing parameters from NuFit 5.3 (I. Esteban et al. 2020, 2024) in the calculation. We see that the flavor fractions at Earth change from $(f_{e,\oplus}, f_{\mu,\oplus}, f_{\tau,\oplus}) \approx (0.33:0.34:0.33)$ to $(0.23:0.40:0.38)$ due to the muon damping. Tau neutrinos appear because of neutrino oscillation.

Again, we emphasize two features of flavor fraction in contrast to that of instantaneous approximation: the transition occurs at relatively larger neutrino energy, and the electron (muon and tau) neutrino fraction does not decrease (increase) to the level of the instantaneous approximation. These are all due to the neutrino production at a radius much larger than R_0.

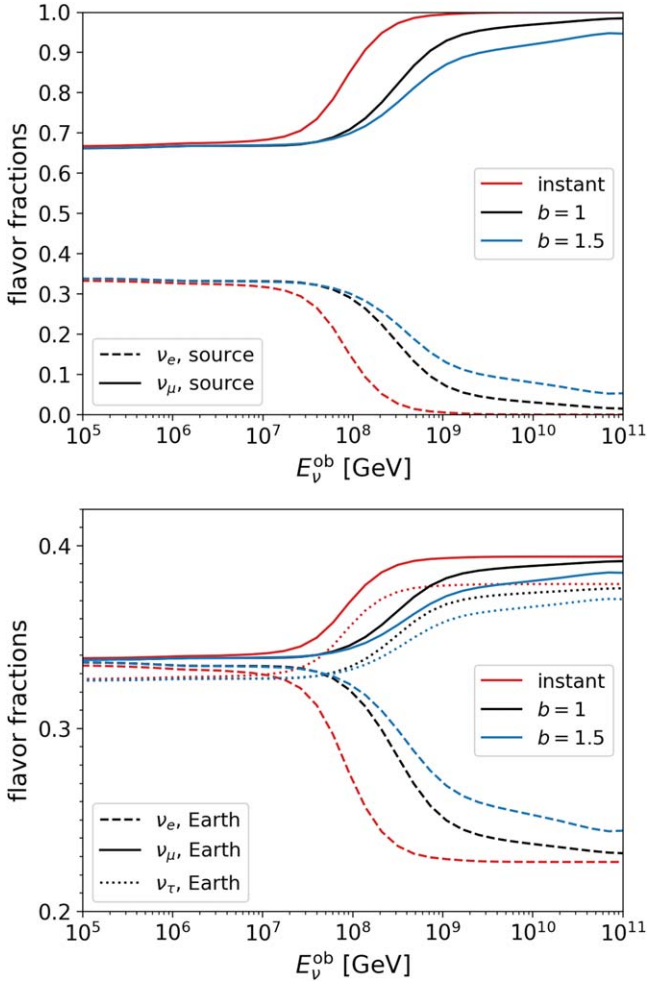

Figure 10. Neutrino flavor fraction as a function of neutrino energy. The upper and lower panels show the flavor fractions in the source and at Earth, respectively. The case of instantaneous approximation (red lines) is shown for comparison.

4. Conclusion and Discussion

In this work, we consider time-evolving and then time-integrated neutrino production in GRB jets during the whole period of the expansion of the jets. We solve continuity equations for nucleons, pions, and muons to account for particle production, cooling, and decay in the evolution. We use the Sim-B model from H10 for numerical calculation of pion production. We find that the jet expansion affects the pion damping effect, resulting in significantly different neutrino spectra for very high-energy neutrinos compared with that of the instantaneous approximation. Under the fiducial parameter setting, our neutrino fluence is significantly higher than that of the instantaneous approximation for neutrinos of $E_\nu^{\rm ob} \gtrsim 1$ EeV; the faster decrease of the magnetic field leads to larger neutrino fluence due to the contribution from large radii (see Figure 7). Moreover, the jet expansion also affects the muon damping effect, and results in different neutrino flavor fractions as a function of neutrino energy (Figure 10), compared to that of the instantaneous approximation. Finally, we also find that the

neutrino fluence at very high energies, say, $\gtrsim$10 EeV, is not sensitive to the dissipation radius R_0 and the jet Lorentz factor Γ, except for the optically thick case (Figures 8 and 9).

The dissipation radius, R_0, is a crucial physical parameter in GRB models, which also affects much of the neutrino spectrum (Figure 8; see also B. Zhang & P. Kumar 2013; Y.-D.-J. Ou et al. 2024). The adopted fiducial value $R_0 = 10^{14}$ cm may correspond to the typical case of the internal-shock model (e.g., M. J. Rees & P. Meszaros 1994), whereas $R_0 = 10^{16}$ cm corresponds to the magnetic-dominated model (e.g., M. Lyutikov & R. Blandford 2003; B. Zhang & H. Yan 2011), and $R_0 = 10^{13}$ cm to the dissipative photosphere model (M. J. Rees & P. Mészáros 2005). As discussed in Section 3.2, the fluence is roughly $\propto R_0$ for PeV neutrinos. The pion damping energy increases with R_0, resulting in similar neutrino fluence for internal-shock and magnetic-dominated models at $E_\nu^{\rm ob} \gtrsim 10^{10}$ GeV. In the dissipative photosphere model, the nucleon cool significantly in small radii and high-energy neutrino production is suppressed. Thus, high-energy neutrino emission can be a probe for the GRB prompt emission model. However, note also that in the framework of internal shocks, there should be residual collisions in larger radii generating X-ray or optical prompt emission (Z. Li & E. Waxman 2008). These additional photons from residual collisions may enhance the neutrino production at high energies, say, the EeV range, by PIs at large radii.

We should also note that some previous works on GRB neutrino emission have considered energy dissipation at a wide range of radii and the contribution to UHE neutrinos (e.g., K. Murase & S. Nagataki 2006; K. Murase et al. 2008; M. Bustamante et al. 2015, 2017). These works show that large dissipation radii have effects on the peak neutrino energy, and generate a high-energy neutrino spectrum that is flatter than the E_ν^{-4} expected in the one-zone model.

Non-detection of GRB neutrinos has put stringent constraints on GRB physical parameters. For the fiducial parameter values, the diffusive neutrino intensity at $\sim$0.1 PeV from GRBs can be estimated by $I_{\nu,\rm GRB} \approx (c/4\pi) f_z \dot{n}_{\rm GRB} t_{\rm H} (E_\nu^{\rm ob})^2 N_\nu^{\rm ob} \sim 3 \times 10^{-11}$ GeV cm^{-2} s^{-1} sr^{-1}, with the local GRB event rate density $\dot{n}_{\rm GRB} \sim 1$ Gpc^{-3} yr^{-1} (e.g., D. Wanderman & T. Piran 2010), $f_z \sim 3$ accounts for the redshift distribution of GRB event rate density (E. Waxman & J. Bahcall 1998), and $t_{\rm H} \sim 10$ Gyr the Universe age. This is smaller than 1% of the diffuse neutrino flux, satisfying the constraint of GRB neutrinos by IceCube observation (R. Abbasi et al. 2022).

EeV neutrinos are largely contributed by the multi-pion channel, which results in the neutrino spectrum increasing slowly with energy above the break $\sim$1 PeV. In the case of fiducial parameter values, the fluence at the spectral peak, around 0.1 EeV, is roughly $\sim$1 GeV cm^{-2}. We can estimate the detection rate of GRBs by the next generation neutrino telescopes, GRAND200k and IceCube-Gen2, which are sensitive to UHE neutrinos. For example, GRAND200k's instantaneous sensitivity is $\sim$0.1 GeV cm^{-2} for EeV neutrinos at zenith angle $\theta_z = 90^\circ$ (see Figure 8 in J. Álvarez-Muñiz et al. 2020); thus, GRBs are detectable up to 300 Mpc, and the GRB detection rate is $\sim 0.1(\Delta\Omega/4\pi)$ yr^{-1}, where $\Delta\Omega$ is the field of view of telescope.

Adiabatic cooling is considered for all charged particles in the calculation in this work. However, the particles with large enough energy may not be confined by the magnetic field of the plasma, e.g., the Larmor radius of protons is $r_{\rm L} \propto E_p/B \propto E_p R^b$, increasing with energy and radius, and may be larger than the size of the plasma for large E_p or R. These protons can propagate free of adiabatic cooling, and contribute more to the neutrino production at large radius, leading to larger neutrino fluence above damping energy than the results in this work. Removal of adiabatic cooling will lead to larger damping energy of muons or pions, especially when adiabatic cooling dominates synchrotron cooling (e.g., the case of Figure 4). If protons did escape, our results can be considered as lower limits to neutrino emission.

We only consider the main neutrino production channel, pion chain decay, in our calculation, but there are other channels in the PIs, e.g., neutron decay and kaon decay (R. Moharana & N. Gupta 2012, and references therein). Neutron decay mainly occurs outside of the source due to the long decay time of neutrons, much longer than any other timescales taken into account in the process. The energy of the electron neutrino from neutron decay is small, i.e., about a fraction $(m_n - m_p)/m_n \sim 10^{-3}$ of the primary neutron, much smaller than that from pion decay and negligible. Kaon decay is the second most important channel for high-energy neutrino production. Due to their heavy mass and short decay time, the damping energy of kaons is 30 times larger than that of pions. Thus, kaon decay can contribute some electron neutrinos to the high-energy region, suffering muon damping.

Acknowledgments

The authors thank Tianqi Huang and Xishui Tian for the helpful discussions. This work is supported in China by National Key R&D program of China (under the grant 2024YFA1611402), the Natural Science Foundation of China (No. 11773003, U1931201) and the China Manned Space Project (CMS-CSST-2021-B11).

Appendix A
Sim-B Model of PIs and Nucleon Cooling

In this work, we follow the Sim-B model in H10 to treat PIs between nucleons (protons and neutrons) and gamma-ray photons and the related nucleon cooling. Note, we do not distinguish protons and neutrons here in PIs and nucleon cooling. As defined in the Sim-B model, the PIs are split into different interaction types (ITs): Pion production is separated into resonant, direct and multi-pion channels; For each channel the interactions are split into ITs according to the photon energy ranges (in the rest frame of the nucleon), where the cross sections, the inelasticities, the multiplicities and pion production rates, etc. are treated separately with different approaches.

Consider the jet propagates to the source-frame radius R. In the rest frame of the jet, if the nucleon number per unit energy interval is $N_p(E_p, R)$, and the photon number per unit energy interval per unit volume is $n_\gamma(\epsilon, R)$, the number production rate of charged pions, including π^+ and π^-, per unit energy interval at pion energy E_π and radius R can be given by following Equation (28) in H10,

$$Q_\pi(E_\pi, R) = \sum_{\rm IT} N_p\left(\frac{E_\pi}{\chi^{\rm IT}}, R\right)\frac{m_p c^3}{E_\pi} \times \int_{\epsilon_{\rm th}/2}^{\infty} dy\, n_\gamma\left(\frac{m_p c^2 y \chi^{\rm IT}}{E_\pi}, R\right) M_\pi^{\rm IT} f^{\rm IT}(y), \quad \text{(A1)}$$

where the sum adds up all ITs, $\epsilon_{\rm th} \simeq 150$ MeV is the threshold, $y \equiv E_\pi \epsilon/\chi^{\rm IT} m_p c^2$, $\chi^{\rm IT}$ is the fraction of the initial nucleon energy deposited in one pion, $M_\pi^{\rm IT}$ is the multiplicity (i.e., the average number of pions that are produced), and $M_\pi^{\rm IT} f^{\rm IT}$ is the production rate of pions with specific function $f^{\rm IT}$ relevant to the cross section.

As protons and neutrons are not distinguished, the PIs are simplified to be a cooling process. The cooling rate of a nucleon, proton, or neutron, with energy E_p due to PIs can be calculated following Appendix B in H10. Given the target photon spectrum $n_\gamma(\epsilon, R)$, the cooling rate of a nucleon at R is

$$t_{p\gamma}^{-1}(E_p, R) = \sum_{\rm IT} \Gamma^{\rm IT}(E_p, R) K^{\rm IT}, \tag{A2}$$

where

$$\Gamma^{\rm IT}(E_p, R) = \int_{\epsilon_{\rm th} m_p c^2/2E_p}^{\infty} d\epsilon\ n_\gamma(\epsilon, R) f^{\rm IT}\left(\frac{E_p \epsilon}{m_p c^2}\right) \tag{A3}$$

is the interaction rate of a nucleon, and $K^{\rm IT}$ is the inelasticity.

For each interaction type IT, the definition of the energy range, and the specific values of $\chi^{\rm IT}$, $M_\pi^{\rm IT}$, $K^{\rm IT,}$ and the cross section can be found in Tables 4, 5, and 6 in H10 for resonant, direct, and multi-pion channels, respectively, and function $f^{\rm IT}$ in Equations (31) and (32) therein for resonances, Equation (33) for direct channels, and Equation (40) for multi-pion channels.

Appendix B
Secondary Spectrum from Weak Decays

For a decay chain $a \to b$, the probability distribution function of secondary particle b, i.e., the normalized particle number per unit energy interval, can be described by $p_{a\to b}(E_b; E_a) = F_{a\to b}(E_b/E_a)/E_a$, where $F_{a\to b}(r)$ is a dimensionless function, with $r = E_b/E_a$. We adopt the forms of $F_{a\to b}(r)$ following P. Lipari et al. (2007). For secondary muons and muon neutrinos from pion decays, we take

$$F_{\pi\to\mu}(r) = \frac{1}{1-r_\pi}\Theta(r - r_\pi), \tag{B1}$$

$$F_{\pi\to\nu_\mu}(r) = \frac{1}{1-r_\pi}\Theta(1 - r_\pi - r), \tag{B2}$$

where $r_\pi = (m_\mu/m_\pi)^2$. For secondary electron and muon neutrinos from muon decays, we take

$$F_{\mu\to\nu_\mu}(r) = \frac{5}{3} - 3r^2 + \frac{4}{3}r^3, \tag{B3}$$

$$F_{\mu\to\nu_e}(r) = 2 - 6r^2 + 4r^3. \tag{B4}$$

Note, because neutrinos and anti-neutrinos are summed up in this work, we have adopted the functions for unpolarized muons.

Appendix C
Instantaneous Approximation for Neutrino Production

In the usual approaches for the calculation of neutrino production in GRB jets, only the contribution within one dynamical time around R_0 is taken into account, not considering the evolution and time integral of the neutrino spectrum during jet expansion. In these kinds of approaches, either a steady-state solution for pion and muon spectra or time-dependent evolution within only one dynamical time is considered (e.g., K. Murase & S. Nagataki 2006; H10, 2012; M. Bustamante et al. 2015, 2017). We would like to call these approaches the "instantaneous approximation" here.

To calculate the neutrino spectrum in the instantaneous approximation, the following approach is adopted. First, to obtain the steady-state solutions for pion and muon spectra at $R = R_0$, respectively, we take

$$N_x(E_x, R_0) = Q_x(E_x, R_0) \min[\tau_x(E_x), t_{x,\rm cool}(E_x, R_0)], \tag{C1}$$

where $x = \pi$ or μ. Note, no adiabatic cooling is considered. The production rates, Q_x's, for pions or muons are calculated in the same way as described in Appendices A and B. Next, the neutrino production rate $Q_\nu(E_\nu, R_0)$ is given by Equation (9), taking the steady-state spectra of pions and muons, $N_x(E_x, R_0)$, in Equation (C1). Finally, the total neutrino spectrum is calculated as multiplied by the dynamical time $t_{\rm dyn}(R_0) = t_0$,

$$N_\nu(E_\nu) = Q_\nu(E_\nu, R_0) t_0. \tag{C2}$$

So in such an approximation, the instantaneous neutrino production rate around R_0 is used, no adiabatic cooling is considered, and the contribution from large radii is ignored.

ORCID iDs

Qinyuan Zhang (张秦源) https://orcid.org/0000-0003-1469-208X

References

Aartsen, M. G., Abbasi, R., Ackermann, M., et al. 2021, JPhG, 48, 060501
Aartsen, M. G., Ackermann, M., Adams, J., et al. 2017, ApJ, 843, 112
Abbasi, R., Abdou, Y., Abu-Zayyad, T., et al. 2010, ApJ, 710, 346
Abbasi, R., Abdou, Y., Abu-Zayyad, T., et al. 2011, PhRvL, 106, 141101
Abbasi, R., Ackermann, M., Adams, J., et al. 2022, ApJ, 939, 116
Álvarez-Muñiz, J., Alves Batista, R., Balagopal V., A., et al. 2020, SCPMA, 63, 219501
Band, D., Matteson, J., Ford, L., et al. 1993, ApJ, 413, 281
Bustamante, M., Baerwald, P., Murase, K., & Winter, W. 2015, NatCo, 6, 6783
Bustamante, M., Heinze, J., Murase, K., & Winter, W. 2017, ApJ, 837, 33
Chiaberge, M., & Ghisellini, G. 1999, MNRAS, 306, 551
Dai, Z. G., & Lu, T. 2001, ApJ, 551, 249
Esteban, I., Gonzalez-Garcia, M. C., Maltoni, M., Schwetz, T., & Zhou, A. 2020, JHEP, 2020, 178
Esteban, I., Gonzalez-Garcia, M. C., Maltoni, M., Schwetz, T., & Zhou, A., 2024 NuFIT 5.3, www.nu-fit.org
Guetta, D., Hooper, D., Alvarez-Muñiz, J., Halzen, F., & Reuveni, E. 2004, APh, 20, 429
He, H.-N., Liu, R.-Y., Wang, X.-Y., et al. 2012, ApJ, 752, 29
Hümmer, S., Baerwald, P., & Winter, W. 2012, PhRvL, 108, 231101
Hümmer, S., Rüger, M., Spanier, F., & Winter, W. 2010, ApJ, 721, 630
IceCube Collaboration, Abbasi, R., Abdou, Y., et al. 2012, Natur, 484, 351
Kashti, T., & Waxman, E. 2005, PhRvL, 95, 181101
Kotera, K., & Olinto, A. V. 2011, ARA&A, 49, 119
Li, Z. 2012, PhRvD, 85, 027301
Li, Z., Dai, Z. G., & Lu, T. 2002, A&A, 396, 303
Li, Z., & Waxman, E. 2007, arXiv:0711.4969
Li, Z., & Waxman, E. 2008, ApJL, 674, L65
Lipari, P., Lusignoli, M., & Meloni, D. 2007, PhRvD, 75, 123005
Lyutikov, M., & Blandford, R. 2003, arXiv:astro-ph/0312347
Mészáros, P., & Rees, M. J. 1997a, ApJ, 476, 232
Mészáros, P., & Rees, M. J. 1997b, ApJL, 482, L29
Moharana, R., & Gupta, N. 2012, Astroparticle Physics, 36, 195
Murase, K., Asano, K., Terasawa, T., & Mészáros, P. 2012, ApJ, 746, 164
Murase, K., Ioka, K., Nagataki, S., & Nakamura, T. 2008, PhRvD, 78, 023005
Murase, K., & Nagataki, S. 2006, PhRvD, 73, 063002
Ou, Y.-D.-J., Lü, H.-J., Chang, X.-Z., Liu, X.-X., & Liang, E.-W. 2024, ApJ, 976, 174
Paczynski, B., & Rhoads, J. E. 1993, ApJL, 418, L5
Paczynski, B., & Xu, G. 1994, ApJ, 427, 708

Rees, M. J., & Meszaros, P. 1994, ApJL, 430, L93
Rees, M. J., & Mészáros, P. 2005, ApJ, 628, 847
Vietri, M. 1995, ApJ, 453, 883
Wanderman, D., & Piran, T. 2010, MNRAS, 406, 1944
Waxman, E. 1995, PhRvL, 75, 386
Waxman, E., & Bahcall, J. 1997, PhRvL, 78, 2292
Waxman, E., & Bahcall, J. 1998, PhRvD, 59, 023002
Waxman, E., & Bahcall, J. 2000, ApJ, 541, 707
Zhang, B. 2019, The Physics of Gamma-ray Bursts (Cambridge: Cambridge Univ. Press),
Zhang, B., & Kumar, P. 2013, PhRvL, 110, 121101
Zhang, B., & Yan, H. 2011, ApJ, 726, 90